CrossMark

Effect of Annealing Temperature on Structural, Optical and Visible-Light Photocatalytic Properties of NiTiO₃ Nanopowders

PHAM PHI HUNG,[1] TRAN TAT DAT,[1] DANG DUC DUNG,[1]
NGUYEN NGOC TRUNG,[1] MAI HONG HANH,[2] DANG NGOC TOAN,[3]
and LUONG HUU BAC [1,4]

1.—School of Engineering Physics, Ha Noi University of Science and Technology, 1 Dai Co Viet, Hanoi, Vietnam. 2.—Faculty of Physics, VNU University of Science, 334 Nguyen Trai, Hanoi, Vietnam. 3.—Institute of Research and Development, Duy Tan University, R.809, K7/25 Quang Trung, Da Nang, Vietnam. 4.—e-mail: bac.luonghuu@hust.edu.vn

Nickel titanate (NiTiO₃) nanopowders have been synthesized using the sol–gel method. The effect of annealing temperatures on the structural, optical, and visible-light photocatalytic properties of the synthesized NiTiO₃ nanopowders was investigated. The nanopowders annealed at a low temperature (500–600°C) showed a mixture of NiO, anatase, rutile, and NiTiO₃. The TiO₂ and NiO phases decreased with increased calcination temperature and transformed to NiTiO₃ phase at a temperature higher than 600°C. The particle size of the prepared samples substantially increased with increased annealing temperature. The reduction of the optical band gap from 2.46 eV to 2.31 eV corresponded to the increase in annealing temperature from 500°C to 900°C, respectively. The NiTiO₃ nanopowders annealed at 500°C exhibited high efficiency in the photodegradation of congo red dye under visible light irradiation.

Key words: NiTiO₃, annealing temperature, ilmenite, sol–gel, photocatalysis

INTRODUCTION

The rapid development of industry and human society poses serious environmental problems. The degradation of industrial organic wastes concerns scientists. In 1972, Fujishima and Honda[1] reported the evolution of oxygen and hydrogen from a TiO₂ electrode under the irradiation of light. Since then, photocatalysis has become the most effective and economical method for decoloring organic waste. TiO₂ materials have been widely investigated for photocatalysis particularly during hydrogen fuel production, detoxification of effluents, disinfection, superhydrophilic self-cleaning, elimination of inorganic/organic gaseous pollutants, and the synthesis of organic fuels.[2–4] Unfortunately, TiO₂ has wide band gap values: 3.2 eV for anatase phase and 3.0 for rutile phase. These wide band gaps prevent the real application of TiO₂ because the material is active only in the UV wavelength. Thus, this material performs poorly in processes associated with solar irradiation because the UV energy in solar radiation is smaller than 5% of the total solar energy. To harvest visible light in solar irradiation, TiO₂ materials have been modified by doping with elemental cations and anions; heterojunctions are created by combining TiO₂ with metals or other semiconductors.[5–8] Generally, doping can narrow the band gap of TiO₂ to allow visible light absorption. The heterojunctions can provide an internal electric field that enhances charge separation and prevents the recombination of electrons and holes caused by illumination.

To date, many photocatalytic materials have been used in the degradation of different organic compounds. The challenges for the application of

photocatalysis must be addressed, and they include photocatalytic activity, development of visible light photocatalysts, the search for alternative photocatalytic materials, and the design and development of photocatalytic reactors based on the irradiation source. Nickel titanate ($NiTiO_3$) is a promising material that has photocatalytic activity under visible light irradiation. Applications of this material in many fields, such as visible-light photocatalysis,[9] solid oxide fuel cells,[10] gas or glucose sensors,[11,12] spin electronic devices with magneto-electric effects,[13] and paint pigments,[14] have been widely investigated owing to its multifunctional ability. $NiTiO_3$ has an ilmenite-type structure with both Ni and Ti possessing octahedral coordination with alternating cation layers occupied by Ni^{2+} and Ti^{4+} alone.[15] $NiTiO_3$ is an n-type semiconductor with a band gap of around 2.18 eV. The low band gap makes $NiTiO_3$ suitable for visible-light-driven photocatalysis to harvest visible light. Furthermore, the band gap is large enough to provide energetic electrons.[16] Recently, $NiTiO_3$ materials have attracted considerable attention because of their high photocatalytic activity under UV irradiation and remarkable activity under visible light.[17–19] Different wet chemical methods, such as polymer pyrolysis,[20] stearic acid gel,[21] Pechini's method,[22] a sonochemical method,[23] and co-precipitation,[18] have been developed to obtain $NiTiO_3$ nanoparticles. The physical and chemical properties of nanoparticles prepared via wet chemical methods are considerably dependent on the annealing temperature which is a major parameter in determining the size, morphology, and phase of the nanoparticles.

The present study aimed to investigate the relationship between annealing temperature and the structural, optical, and visible-light photocatalytic activity of $NiTiO_3$ nanopowders. The photocatalytic activity of $NiTiO_3$ annealed at 500–900°C to decolorize congo red (CR) organic dye was measured. The results showed that the photocatalytic activity of the samples changed substantially with a change in annealing temperature. The sample annealed at a low annealing temperature had improved photocatalytic activity under visible-light irradiation.

EXPERIMENTAL

The $NiTiO_3$ nanoparticles were synthesized using the sol–gel technique. The raw materials used were tetraisopropoxytitanium (IV) ($C_{12}H_{28}O_4Ti$) and nickel nitrate ($Ni(NO_3)_2 \cdot 6H_2O$). A citric acid ($C_6H_8O_7$) solution (C_M = 1.5 mol/L) was the solvent. The experimental procedure for the synthesis of $NiTiO_3$ samples was as follows. First, the $C_{12}H_{28}O_4Ti$ was dissolved in the $C_6H_8O_7$ solution at 70°C. A transparent homogeneous sol was formed after stirring vigorously for 2 h. Then, $Ni(NO_3)_2 \cdot 6H_2O$ with equal moles of Ni and Ti was introduced. The resulting solution was stirred for about 4 h to obtain a gel. The gel was oven-dried at

120°C to obtain a xerogel, which was fired at 400°C for 2 h and annealed from 500°C to 900°C for 3 h. X-ray diffraction (XRD) patterns were recorded on a Philips X'PertPro x-ray diffractometer using a Ni-filtered CuKα radiation at a scan range of 20°–70°. Field-emission scanning electron microscopy images were obtained on a JEOL JSM-7600F. UV absorbances were determined on a UV–Vis–NIR spectrophotometer (Perkin-Elmer Lambda 1050). The Raman spectra were recorded on a micro-Raman spectrophotometer (JASCO Raman NRS-3000) using a 633-nm excited laser at room temperature.

Photocatalytic measurements were carried out in an aqueous CR solution to evaluate the photocatalytic activity of the fabricated powders. A mixture of 40 mg NTO powder and 40 mL CR solution (10^{-4} mol/L) was sonicated for 10 min and stirred for 30 min in a quartz tube in the dark to reach the adsorption/desorption equilibrium for the CR and oxygen on the surface of the NTO powder. The stirred suspension was then illuminated by a 50-W phase LED lamp (Model D CP03L/50 W; RALACO). The spectrum of the light source is presented in Fig. S1. The light source was placed about 15 cm from the solution for the visible-light reaction. The quartz tube was exposed to air during the reaction to ensure sufficient dissolved oxygen in the solution. At an interval of 30 min, 3 mL of the suspension was extracted from the tube and centrifuged (4000 rpm, 15 min). The supernatants were analyzed by recording the variations of the absorption band maximum in the UV–Vis spectra using a Cary UV–Vis spectrophotometer. The quantitative determination of CR was performed by measuring its maximum absorption of UV–Vis at 500 nm. A blank reaction was carried out following the same procedure without adding a catalyst. The photodegradation ratio was calculated using Eq. 1:

$$\text{Degradation ration } (\%) = \frac{C_o - C}{C_o} \times 100, \qquad (1)$$

where C_o is the absorbance of CR dye before irradiation, and C is the absorbance of CR under diffraction irradiation time intervals.

RESULTS AND DISCUSSION

Annealing is a common treatment used to improve the crystallinity of ceramic materials synthesized via wet chemical methods. Figure 1 shows the XRD patterns for the synthesized powders annealed at 500–900°C for 3 h. All samples included the diffraction peaks at 2θ = 24.03°, 32.99°, 35.55°, 40.76°, 49.34°, 53.90°, 57.35°, 62.35°, and 63.97°, corresponding to the lattice planes of (012), (104), (110), (113), (024), (116), (018), (214), and (300), respectively. These values indicate the ilmenite structure. The observed peaks and corresponding planes were well-matched with the standard JCPDS file no-83-0198, which represents the rhombohedral crystal structure with a R3 space group. However,

Effect of Annealing Temperature on Structural, Optical and Visible-Light Photocatalytic
Properties of NiTiO$_3$ Nanopowders

7303

the impurity phases of anatase, rutile TiO$_2$ and NiO were observed in the samples annealed at a temperature below 600°C. At a sintering temperature of 500°C, the diffraction peaks belonging to the impurity phases had high intensity, indicating high contents of TiO$_2$ and NiO (Fig. 1b). The diffraction peaks of these phases gradually decreased, indicating decreased TiO$_2$ impurity and phase transition to NiTiO$_3$. At annealing temperatures above 600°C, the diffraction of the impurity phases was not visible. This result indicated that the NTO phase was pure at such annealing temperatures. The NiTiO$_3$ phase did not form when the powder was annealed at a temperature lower than 500°C (Supplementary Fig. S2). Furthermore, the diffraction intensity of NTO ceramics increased with increased annealing temperature. This behavior indicated an enhancement in the crystallinity of the NTO samples at increased sintering temperature.

The results of XRD analysis indicated that pure NTO phase was obtained when the samples were annealed at a temperature higher than 600°C. To corroborate the results of the XRD analysis, Raman spectroscopy was used to analyze the vibration properties of the fabricated powders. Figure 2a shows the Raman scattering of NiTiO$_3$ samples annealed at different temperatures. The theoretical calculation predicted that the optical normal modes of vibrations at the Brillouin zone center have symmetries represented by $5A_g + 5E_g + 4A_u + 4E_u$, where $5A_g + 5E_g$ are ten active Raman modes, $4A_u + 4E_u$ are inference active modes, and $A_u + E_u$ are two modes inactive in both Raman and inference modes.[24–26] Therefore, ten Raman active modes are expected, with each E_g mode being twofold degenerated to $E_g^1 + E_g^2$ along with the eight IR active modes $4A_u + 4E_u$.[26] Preciado et al.[27] predicted that the band located at 720 cm^{-1} corresponds to the Ti–O–Ti vibration of the crystal structure.

Vijayalakshmi et al. pointed out that the bands located at 617 cm^{-1} and 690 cm^{-1} originate from the stretching of Ti–O and bending of O–Ti–O bonds, whereas the band at 547 cm^{-1} results from Ni–O bonds.[28] The vibration modes are localized at 631.9 cm^{-1} and 760.5 cm^{-1}, which resulted from the stretching vibrations of TiO$_6$ and octahedral vibrations in the region 500–830 cm^{-1}.[20] In addition, Preciado et al. pointed out that the E_g mode at 227.6 cm^{-1} can be considered as the asymmetric breathing vibration of the oxygen octahedral; the ones at 290.2 cm^{-1} and 434.3 cm^{-1} can be described by the twist of the oxygen octahedral due to the vibrations of the Ni and Ti atoms parallel to the xy plane; and the E_g modes at 463.4 cm^{-1} and 609.7 cm^{-1} are assigned to the asymmetric breathing and twist of the oxygen octahedral with the cationic vibrations parallel to the xy plane.[26] Our result indicated that the Raman spectra were considerably dependent on the annealing temperatures. The ten prominent Raman active modes were observed in the NiTiO$_3$ ceramics annealed at above 600°C. These results confirmed the rhombohedral structure and corroborated the recent reports. At annealing temperatures of 500 and 550°C, the Raman vibration mode of the anatase phase of TiO$_2$ was clearly observed in the samples with E_g mode at 145 cm^{-1}, 515 cm^{-1}, and 635 cm^{-1}.[29] The intensity of the E_g mode at 145 cm^{-1} for the sample annealed at 600°C strongly decreased. This mode disappeared completely for the sample annealed at temperatures higher than 600°C. Similarly, the vibration mode at 635 cm^{-1} gradually disappeared at high annealing temperatures. The vibration mode relating to rutile TiO$_2$ phase was not detected by the specific vibration mode in the Raman spectra. Only one vibration mode of this phase at 145 cm^{-1} was observed; however, this mode overlapped with that of the anatase phase. This result suggested the
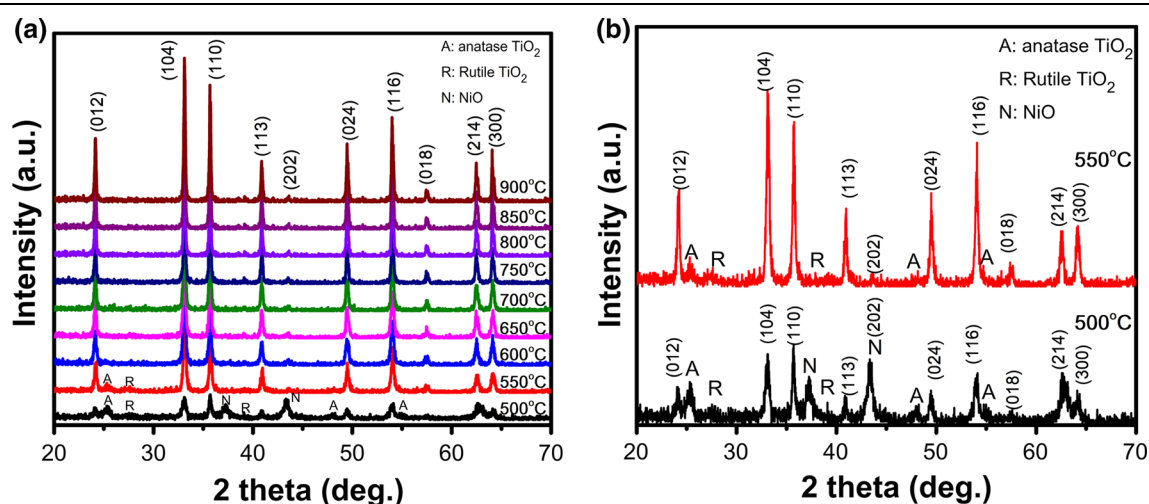

Fig. 1. (a) XRD pattern of NiTiO$_3$ annealed at different temperatures from 500°C to 900°C and (b) XRD pattern of NiTiO$_3$ annealed at 500°C and 550°C.
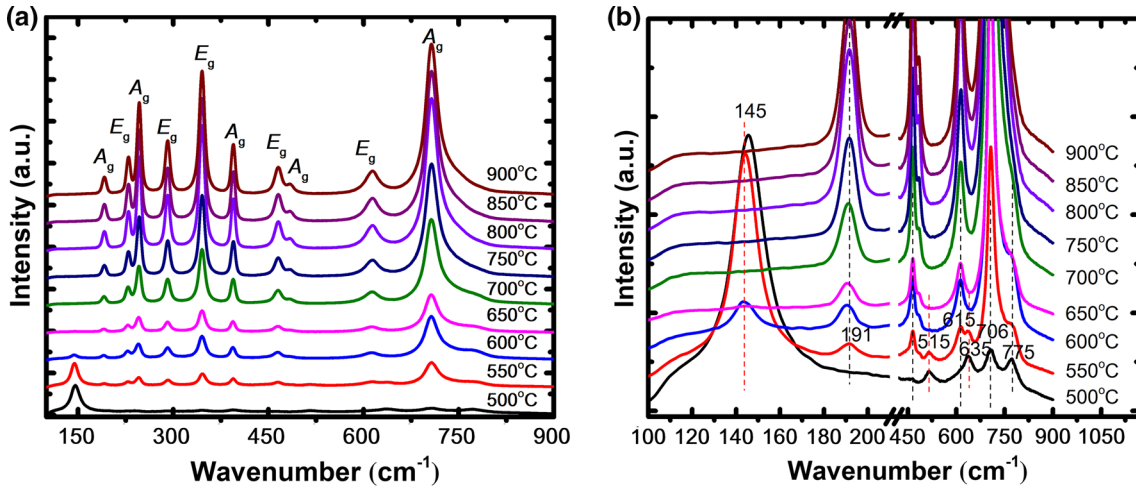
Fig. 2. Raman spectra of (a) NiTiO$_3$ annealed at different temperatures from 100 cm^{-1} to 900 cm^{-1} and (b) zoom in from 100 cm^{-1} to 250 cm^{-1} and from 430 cm^{-1} to 900 cm^{-1}.

presence of a minute quantity of rutile TiO$_2$ in the fabricated samples annealed at low temperatures. The results of Raman spectral analysis corroborated the results of XRD analysis, which confirmed the phase transition from TiO$_2$ impurity to NTO phase. Hence, pure NTO can be obtained at an annealing temperature higher than 600°C. In addition, the increase in Raman vibration band intensity with increased annealing temperature from 500 to 900°C indicated that thermal annealing resulted in improved crystallinity.

Figure 3a–e shows the surface morphology of NiTiO$_3$ annealed at different temperatures from 500°C to 900°C. Figure 3f shows the dependence of particle size on annealing temperature. The particle size increased quickly with increasing annealing temperature. The particle sizes were around 18 and 138 nm for the samples annealed at 500 and 900°C, respectively (Fig. 3f). This phenomenon is normal in ceramic materials. The particles in all the samples had irregular shapes. The particles showed a homogeneous distribution at an annealing temperature of 700°C. The increase in annealing temperature promotes the coalescence among the particles. The particles are increasingly sintered and had different sizes when the NTO powders were annealed at 900°C.

Figure 4a shows the optical absorption spectroscopy of NiTiO$_3$ annealed at 500–900°C. The absorption band can be separated into three ranges which are the main absorbance edges around 300–580 nm and two absorbance humps in the ranges 650–1000 nm and 1000–1600 nm. The absorption spectra of the fabricated powders annealed at above 600°C fitted perfectly with the spectral features of Ni^{2+} (3d^8 ion) in octahedral coordination with a first sharp or narrow band in the blue region around 450 nm [v3:3A_{2g} (3F) → 3T_{1g} (3P)], a second broad band in the red region centered around 750–850 nm

[v2:3A_{2g} (3F) → 3T_{1g} (3F)], and a third broad band in the near IR centered between 1200 and 1400 nm [v1:3A_{2g} (3F) → 3T_{2g} (3F)].[30,31] The absorption shoulders at around 512 nm may be tentatively assigned to the spin-forbidden transitions 1A_{1g} (1G) + 1T_{2g} (1D).[31] The first high-intensity absorption band in the near UV (around 365 nm) was associated with the typical charge-transfer transitions O^{2-}–Ti^{4+}. Our results agreed with recently reported optical properties of NiTiO$_3$ materials, where the absorbance peaks resulted from charge transfer from Ni^{2+} to Ti^{4+} caused by the spin-splitting of Ni ions under the crystal field.[32] The increased annealing temperature resulted in the gradual increase of absorption intensity (increased optical density) at 454 nm. However, the energy position of this band remained the same, indicating no substantial variation in the Ni–O distances. The determination of the optical band gap energy of the ilmenite structure was recently reported. The theoretical prediction for the NiTiO$_3$ materials has indirect transition, whereas the experimental value was estimated from direct transition.[33,34] The optical band gap energy (E_g) was estimated by using the Wood and Tauc method. E_g values are associated with the absorbance and photon energy by the following equation, $(\alpha h v) \sim (h v - E_g)^n$, where α is the absorbance coefficient, h is the Planck's constant, v is the frequency, E_g is the optical band gap, and n is a constant associated with different types of electronic transition (n = 1/2, 2, 3/2, and 3 for direct allowed, indirect allowed, direct forbidden, and indirect forbidden transitions, respectively). The $(\alpha h v)^2$ as a function of photon energy ($h v$) were plotted (Fig. 4b). The optical band gap values were estimated via extrapolation. For NiTiO$_3$ materials, the largest band gap is expected to relate to the direct electronic transition between the upper edge of the O 2p valence band and the lower edge of the
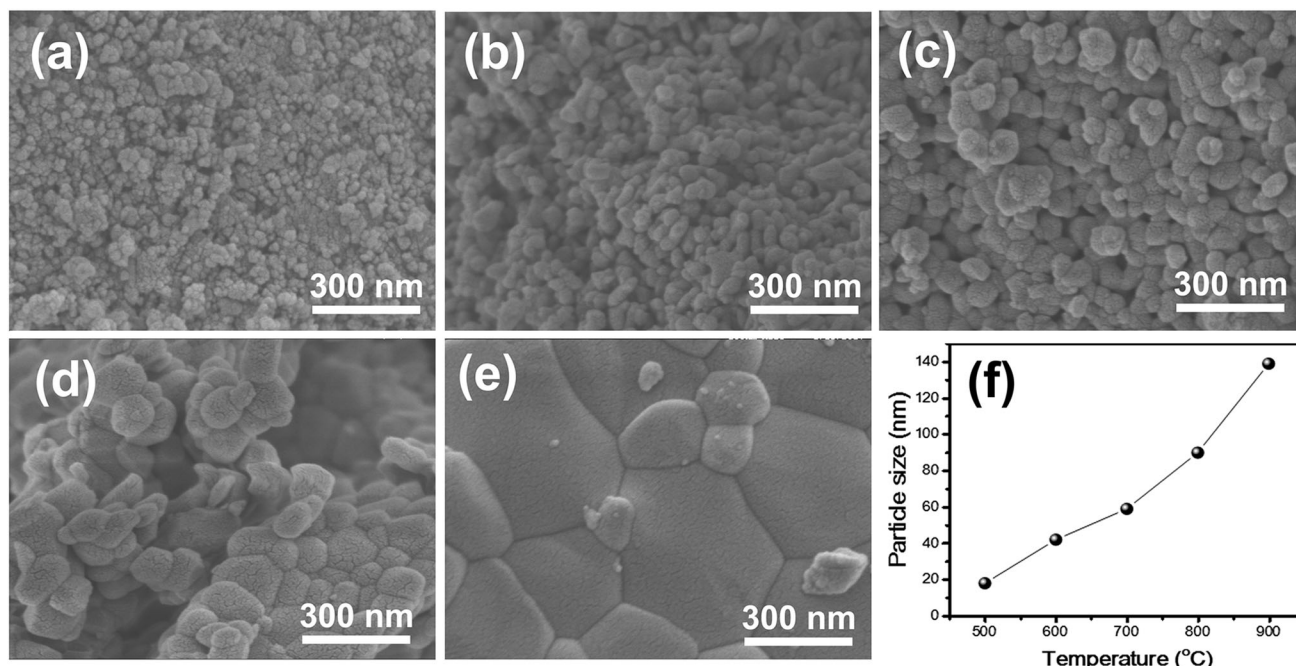
Effect of Annealing Temperature on Structural, Optical and Visible-Light Photocatalytic Properties of NiTiO$_3$ Nanopowders

7305

Fig. 3. FE-SEM images of NiTiO$_3$ annealed at different temperatures: (a) 500°C, (b) 600°C, (c) 700°C, (d) 800°C, (e) 900°C and (f) the dependence of particle size on annealing temperature.
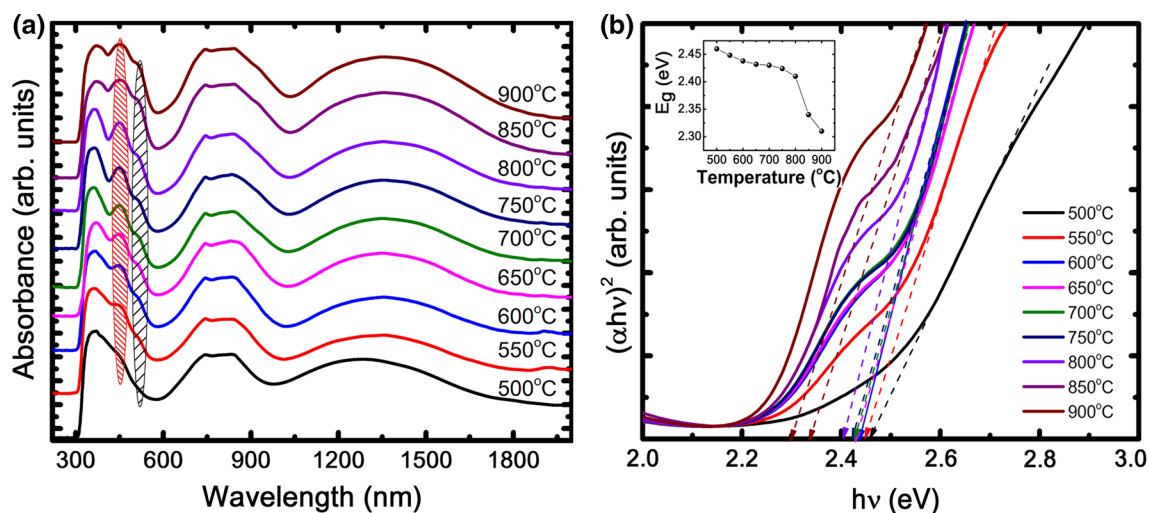

Fig. 4. (a) Optical absorbance spectra and (b) the $(\alpha h\nu)^2$ on photon energy ($h\nu$) of NiTiO$_3$ annealed at different temperatures. Inset in (b) is the dependence of the optical bandgap on annealing temperature.

Ti $3d$ conduction band. The NiTiO$_3$ samples annealed at 900°C exhibited a direct band gap value of 2.31 eV. This value is the smallest optical band gap for all the samples. The results were consistent with the observed direct band gap value of NiTiO$_3$ fabricated by chemical methods. The results showed that the value of the optical band gap tends to increase when the annealing temperature decreases. Generally, the band gap value decreases with the increasing crystalline size.[35] The highest band gap value for the sample annealed at 500°C

was 2.46 eV, which can be caused by the impurity of the TiO$_2$ phase and the small crystalline size. The transformation of TiO$_2$ impurity into a pure NiTiO$_3$ phase of large crystalline size when nanopowders were annealed at high temperature could result in a considerably decreased band gap value.

Figure 5 shows the CR concentration versus irradiation time at different annealing temperatures for the NiTiO$_3$ samples under visible light. The photodegradation of CR was considerably dependent on the annealing temperature. The

NTO sample annealed at 500°C exhibited the fast decomposition activity (about 80%) of CR in the first 2 h, and then the rate gradually decreased. The reduction rate of decomposition for the 550°C annealed sample was much slower than that of the 500°C sample, only 35% after 2 h of light irradiation. However, the reduction rate was still high after 2 h of reaction. The degradation percentage of the 550°C annealed sample after 5 h was 74%. The decoloration activity of the 600°C annealed sample was similar to that of the 550°C sample. Nevertheless, the steeply decreased degradation occurred with the sample annealed at higher than the samples we analyzed above in that both the phase and particle size of the materials changed when the a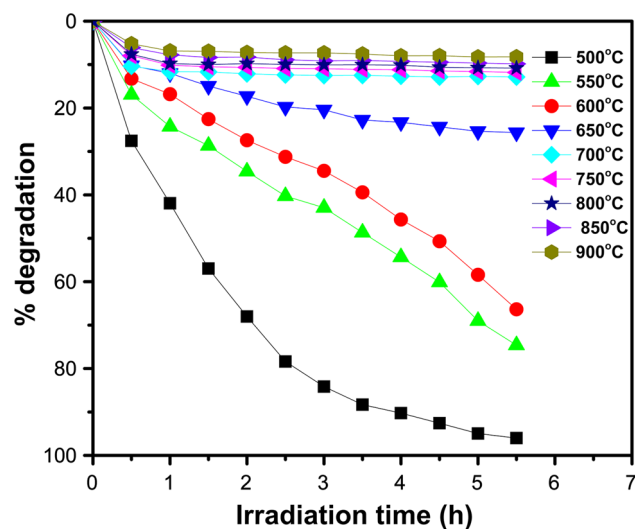nnealing temperature increased from 500°C to 600°C. The good activity in the degradation of CR under irradiation can be due to the small particle size and/or TiO_2-coupled $NiTiO_3$. The coexistence of the $NiTiO_3$ crystalline phase and TiO_2 phase enhanced the percentage removal of CR. A similar behavior was reported for a TiO_2-coupled ilmenite nickel titanate prepared via precipitation in an aqueous medium in the degradation of methylene blue under visible light irradiation.[18] The decreasing photocatalytic activity upon increasing annealing temperature has also been observed by our group in $Bi_{0.5}K_{0.5}TiO_3$ ceramics.[36] Generally, a photocatalytic cycle comprises three steps: (1) Illumination induces transition of electrons from the valence band to the conduction band, leaving an equal number of vacant sites (holes); (2) the excited electrons and holes migrate to the surface; and (3) they react with absorbed electron donors and electron acceptors.[37] In the second step, a large proportion of electron–hole pairs recombine, dissipating the input energy in the form of heat or emitted light. This phenomenon causes the decrease in the photocatalytic activity of the materials. The heterojunctions formed between the two semiconductors can provide an internal electric field that facilitates the separation of the electron–hole pairs and induces fast carrier migration. Such fast migration reduces the recombination of electrons and holes in the second step, resulting in a large number of active species in the hybrid system and an excellent photocatalytic activity. Therefore, the high photocatalytic activity of NTO annealed at low temperature can result from the heterojunction formation (NTO, TiO_2, and NiO) and small particle size of the fabricated powder.

To have a visualized comparison, the kinetic degradation of CR on the surface of the $NiTiO_3$ catalysts annealed at different temperatures was

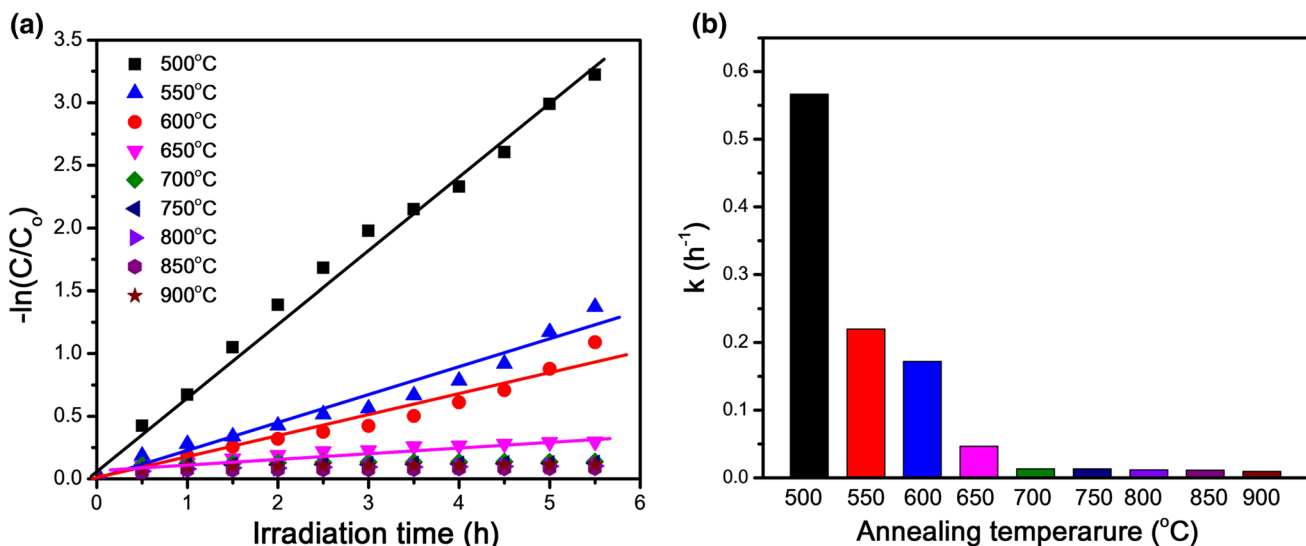Fig. 5. Photocatalytic degradation of CR under visible light irradiation.

Fig. 6. (a) First-order kinetics plot for the photodegradation of CR by NTO ceramics under visible-light irradiation; (b) degradation rate constant k (h^{-1}) for the photodegradation of CR by NTO.

Effect of Annealing Temperature on Structural, Optical and Visible-Light Photocatalytic
Properties of NiTiO$_3$ Nanopowders

7307

calculated. The experimental data were fitted to a first-order model as expressed by Eq. 2.[38]

$$\ln(C_o/C) = -kt, \qquad (2)$$

where k is the rate constant (h^{-1}), and C_o and C are the initial concentration and the concentration at time t of the CR aqueous solution, respectively. As shown in Fig. 6a, the photocatalytic degradation curves of the samples annealed at a temperature lower than 650°C fitted well with pseudo-first-order kinetics. The kinetic constant k was calculated, and the values are presented in Fig. 6b. The kinetic constants of CR photodegradation substantially decreased with increased annealing temperature, while with the increased annealing temperature, the kinetic constant of NTO decreased from the maximum value of 0.567 h^{-1} (sample annealed at 500°C) to 0.013 h^{-1} (sample annealed at 650°C). These results confirmed that the NTO sample annealed at low temperature efficiently enhanced the photocatalytic capability under visible-light irradiation. The enhanced photocatalytic activity was mainly ascribed to the enhanced separation efficiency of photoinduced electron–hole pairs and increased visible-light absorption on the surface due to the small size of the nanoparticles. The electron–hole pair separation was caused by the heterojunction formation between the NTO and the phases of TiO$_2$ and NiO.

CONCLUSIONS

The effect of annealing temperature on the structural, optical, and photocatalytic properties of NiTiO$_3$ nanoparticles fabricated by the sol–gel method was investigated. The NiTiO$_3$ nanoparticles were obtained in pure phase when annealed at a temperature higher than 600°C for 3 h. The NiTiO$_3$ with anatase and rutile phases of TiO$_2$ and NiO existed at a temperature lower than 600°C. The reduction of optical band gap from 2.46 to 2.31 eV corresponded to the increase in annealing temperature from 500°C to 900°C. The increased annealing temperature resulted in substantially decreased photocatalytic activity in the photodegradation of CR dye. The nanopowders annealed at 500°C exhibited CR degradation under visible-light irradiation. The CR degradation was about 80% after visible-light irradiation for 2 h. This result suggests that the nanopowders annealed at a low temperature have a high potential for photocatalytic applications under visible light.

ACKNOWLEDGEMENT

ELECTRONIC SUPPLEMENTARY MATERIAL

The online version of this article (https://doi.org/10.1007/s11664-018-6668-9) contains supplementary material, which is available to authorized users.

REFERENCES

1. A. Fujishima and K. Honda, *Nature* 238, 37 (1972).
2. S.C. Roy, O.K. Varghese, M. Paulose, and C.A. Grimes, *ACS Nano* 4, 1259 (2010).
3. K. Hashimoto, H. Irie, and A. Fujishima, *Jpn. J. Appl. Phys.* 44, 8269 (2005).
4. R. Wang, K. Hashimoto, A. Fujishima, M. Chikuni, E. Kojima, A. Kitamura, M. Shimohigoshi, and T. Watanabe, *Adv. Mater.* 10, 135 (1998).
5. R. Dhabbe, A. Kadam, P. Korake, M. Kokate, P. Waghmare, and K. Garadkar, *J. Mater. Sci. Mater. Electron.* 26, 554 (2014).
6. S. Sato, R. Nakamura, and S. Abe, *Appl. Catal. A Gen.* 284, 131 (2005).
7. S.R. Gul, M. Khan, Z. Yi, B. Wu, and U. Fawad, *J. Electron. Mater.* 46, 6440 (2017).
8. T.T. Dat, P.H. Hung, D.N. Toan, D.D. Dung, C.X. Quan, and L.H. Bac, *Vietnam J. Sci. Technol.* 56, 119 (2018).
9. P. Jing, W. Lan, Q. Su, M. Yu, and E. Xie, *Sci. Adv. Mater.* 6, 434 (2014).
10. Z. Wang, Z. Wang, W. Yang, R. Peng, and Y. Lu, *J. Power Sources* 255, 404 (2014).
11. E. Della Gaspera, M. Pujatti, M. Guglielmi, M.L. Post, and A. Martucci, *Mater. Sci. Eng. B* 176, 716 (2011).
12. K. Huo, Y. Li, R. Chen, B. Gao, C. Peng, W. Zhang, L. Hu, X. Zhang, and P.K. Chu, *ChemPlusChem* 80, 576 (2015).
13. K. Jaye and C. Moureen, *Phys. Rev. B* 93, 104404 (2016).
14. J.-L. Wang, Y.-Q. Li, Y.-J. Byon, S.-G. Mei, and G.-L. Zhang, *Powder Technol.* 235, 303 (2013).
15. S. Yuvaraj, V.D.D. Nithya, K.S. Fathima, C. Sanjeeviraja, G.K. Selvan, S. Arumugam, and R.K. Selvan, *Mater. Res. Bull.* 48, 1110 (2013).
16. Y. Qu, W. Zhou, L. Jiang, and H. Fu, *RSC Adv.* 3, 18305 (2013).
17. A. Srinivas, F. Boey, T. Sritharan, D.W. Kim, K.S. Hong, and S.V. Suryanarayana, *Ceram. Int.* 30, 1431 (2004).
18. S. Xin, H. Jing, and C. Dong, *Ind. Eng. Chem. Res.* 47, 4750 (2008).
19. M.S. Sadjadi, M. Mozaffari, M. Enhessari, and K. Zare, *Superlattices Microstruct.* 47, 685 (2010).
20. K.P. Lopes, L.S. Cavalcante, A.Z. Simões, J.A. Varela, E. Longo, and E.R. Leite, *J. Alloys Compd.* 468, 327 (2009).
21. M.S.S. Sadjadi, K. Zare, S. Khanahmadzadeh, and M. Enhessari, *Mater. Lett.* 62, 3679 (2008).
22. T.-T. Pham, S.G. Kang, and E.W. Shin, *Appl. Surf. Sci.* 411, 18 (2017).
23. N. Pugazhenthiran, K. Kaviyarasan, T. Sivasankar, A. Emeline, D. Bahnemann, R.V. Mangalaraja, and S. Anandan, *Ultrason. Sonochem.* 35, 342 (2017).
24. Y. Fujioka, J. Frantti, A. Puretzky, and G. King, *Inorg. Chem.* 55, 9436 (2016).
25. G. Busca, G. Ramis, J.M.G. Amores, V.S. Escribano, and P. Piaggio, *J. Chem. Soc. Faraday Trans.* 90, 3181 (1994).
26. M.A. Ruiz-Preciado, A. Bulou, M. Makowska-Janusik, A. Gibaud, A. Morales-Acevedo, and A. Kassiba, *CrystEngComm* 18, 3229 (2016).
27. M.A. Ruiz Preciado, A. Kassiba, A. Morales-Acevedo, and M. Makowska-Janusik, *RSC Adv.* 5, 17396 (2015).
28. C. Ecjhao, *E J. Chem.* 9, 282 (2012).
29. N.T. Nolan, M.K. Seery, and S.C. Pillai, *J. Phys. Chem. C* 113, 16151 (2009).
30. G.R. Rossman, R.D. Shannon, and R.K. Waring, *J. Solid State Chem.* 39, 277 (1981).

31. M. Llusar, E. García, M.T. García, V. Esteve, C. Gargori, and G. Monrós, *J. Eur. Ceram. Soc.* 35, 3721 (2015).
32. Y.J. Lin, Y.H. Chang, W.D. Yang, and B.S. Tsai, *J. Non Cryst. Solids* 352, 789 (2006).
33. X. Zhang, B. Lu, R. Li, C. Fan, Z. Liang, and P. Han, *Mater. Sci. Semicond. Process.* 39, 6 (2015).
34. M.A. Ruiz-Preciado, A. Kassiba, A. Gibaud, and A. Morales-Acevedo, *Mater. Sci. Semicond. Process.* 37, 171 (2015).

35. Y. Tong, J. Fu, and Z. Chen, *J. Nanomater.* 2016, 1 (2016).
36. L.H. Bac, L.T.H. Thanh, N. Van Chinh, N.T. Khoa, D. Van Thiet, T. Van Trung, and D.D. Dung, *Mater. Lett.* 164, 631 (2016).
37. H. Tong, S. Ouyang, Y. Bi, N. Umezawa, M. Oshikiri, and J. Ye, *Adv. Mater.* 24, 229 (2012).
38. J. Li, Y. Liu, H. Li, and C. Chen, *J. Photochem. Photobiol. A Chem.* 317, 151 (2016).